A Slewing Control Experiment for Flexible Structures

Jer-Nan Juang* and Lucas G. Horta†
NASA Langley Research Center, Hampton, Virginia
and
Harry H. Robertshaw‡
Virginia Polytechnic Institute and State University, Blacksburg, Virginia

A hardware setup has been developed to study slewing control for flexible structures including a steel beam and a solar panel. The linear optimal terminal control law is used to design active controllers that are implemented in an analog computer. The objective of this experiment is to demonstrate and verify the dynamics and optimal terminal control laws as applied to flexible structures for large-angle maneuver. Actuation is provided by an electric motor while sensing is given by strain gages and angle potentiometers. Experimental measurements are compared with analytical predictions in terms of modal parameters of the system stability matrix, and sufficient agreement is achieved to validate the theory.

Introduction

THE operational success of the NASA Space Shuttle has prompted plans to launch deployable or erectable spacecraft such as the space station, large antennae, etc., which are much larger and more complex than today's spacecraft. One essential characteristic of these space structures is that their structural frequencies fall within the bandwidth of required control systems for fine pointing and retargeting. Questions thus arise as to how to control such large flexible space structures. There are a variety of theoretical approaches to control flexible structures.[1] Experimental validation of control laws, however, has progressed more slowly. References 2-6 offer examples of laboratory implementation to either validate theoretical control concepts for practical application or determine the reason for difficulties and ineffectiveness in control strategies. The experiments in Refs. 2-5 were performed to actively damp vibrational motion of flexible structures. A hardware experiment for maneuvering a flexible beam from one angle to another was first reported in Ref. 6, using an open-loop control method. Yet a large-angle maneuver of flexible structures using closed-loop control methods has not been successfully demonstrated experimentally.

The objective of the present experiment is the demonstration of slewing flexible structures in a single axis while simultaneously suppressing vibration motion by the end of the maneuver. The single-axis slewing experiment is designed to verify theoretical analyses concerning application of modern control methods to the control of flexible structures. The linear optimal control algorithm with terminal constraints in finite time presented in Refs. 7 and 8 is implemented on experimental hardware via an analog computer. The procedure for this experiment involves several distinct steps. First, a structural model is developed, including a rigid body rotation and a finite number of assumed modes. Second, a controller is designed, including actuator and sensor dynamics to simulate the closed-loop response. Third, the control loop is implemented on an analog computer that is interfaced with the experimental apparatus. Fourth, the slewing control algorithm is tested.

A number of different test cases are conducted using open-loop and closed-loop control laws for slewing a steel beam and a solar panel. The primary purpose of open-loop control tests is to examine and adjust the analytical system model used in control law designs. The open-loop results are not reported since they appear to have no practical application. Analytical and experimental results of three different closed-loop controllers are discussed and compared in terms of modal parameters.

Experiment Setup

Two different test models are used for experimental validation (see Fig. 1). The first is a 3.3-ft-long steel beam with a cross section of 3 in. × 0.032 in. The second is a 12.8-ft-long solar panel (aluminum/honeycomb) with a cross section of 2.1 ft × 0.13 in.[9] Both models are instrumented as shown in the sketch of Fig. 1. The instrumentation consists of three full-bridge strain gages to measure bending moments and two angular potentiometers to measure the angle of rotation. The strain gages are located at the root, at 22% of the beam length, and at the midspan. They are calibrated by straining the beam to a known value to obtain the conversion factor. The calibreated value is very close to the calculated value based on the specification sheet. Each model is cantilevered in a vertical plane and allowed to rotate in the horizontal plane by an electric motor. The analog signals from all four sensors are amplified and then monitored by the analog computer and data acquisition system. For further analyses, the data are filtered to remove any frequency components above 50 Hz and then digitally stored. The analog computer closes the control loop and generates a voltage signal for the motor through a voltage amplifier. Two limit switches are also used to limit the angle of rotation in each model to avoid system damage.

System Dynamics

The design of an active controller begins with the construction of a mathematical model of the system to be controlled. The model describes the major features of the real system, including the dynamics of the beam and the actuator, and measurement characteristics of sensors.

Received Oct. 21, 1985; revision received March 10, 1986.

*Senior Research Scientist, Structural Dynamics Branch. Member AIAA.

†Aerospace Engineer, Structural Dynamics Branch. Member AIAA.

‡Associate Professor, Department of Mechanical Engineering.

Beam Dynamics

Both test apparatuses are mathematically modeled as a flexible beam slewing about a vertical axis. The flexible beam is cantilevered from the motor at the root $x=0$ and free at the tip $x=\ell$. The development of the model is based on the classical vibration theory,[10] with a discretization technique as used in Refs. 11-13. By denoting EI the bending rigidity, ρ the mass density of the beam per unit length, y the bending deflection in the horizontal plane, and θ the root angle, the kinetic energy T and potential energy V can be expressed as

$$2T=\int_0^\ell \rho(x\dot{\theta}+\dot{y})^2\mathrm{d}x=I_b\dot{\theta}^2+2\int_0^\ell \rho x\dot{y}\mathrm{d}x\dot{\theta}+\int_0^\ell \rho\dot{y}^2\mathrm{d}x \tag{1}$$

$$2V=\int_0^\ell EIy,_{xx}^2\mathrm{d}x \tag{2}$$

where $t=$ time, $(\dot{})=\mathrm{d}(\,)/\mathrm{d}t$, $(\,),_{xx}=\partial^2(\,)/\partial x^2$ and $I_b=\int_0^\ell \rho x^2\mathrm{d}x$. The Lagrangian L is defined as

$$L=T-V \tag{3}$$

The generalized Hamiltonian principle is used to derive the equation of motion, i.e.,

$$\delta\int_{t_0}^{t_f}[L+W_{\mathrm{nc}}]\mathrm{d}t=0 \tag{4}$$

where the virtual work of a dissipative torque τ applied at the root of the beam is given by

$$\delta W_{\mathrm{nc}}=-\tau\delta\theta \tag{5}$$

and t_f and t_0 represent terminal time and initial time, respectively.

To solve the distributed parameter system, consider the discretization

$$y(x,t)=\sum_{i=1}^{n} q_i(t)\phi_i(x) \tag{6}$$

in which $\phi_i(x)$ are known shape functions of the spatial coordinates linearly independent over the domain $0\le x\le\ell$, $q_i(t)$ are unknown functions of time t, and n is a selected integer. Hence, the variation of the bending displacement has the form

$$\delta y=\sum_{i=1}^{n}\phi_i\delta q_i \tag{7}$$

Introducing Eqs. (5) and (7) into the generalized Hamilton principle, Eq. (4), leads to

$$m\ddot{q}+kq=b\tau \tag{8}$$

where

$$m=\begin{bmatrix} I_b & \int_0^\ell \rho x\phi_i(x)\mathrm{d}x \\ \int_0^\ell \rho x\phi_j(x)\mathrm{d}x & \int_0^\ell \rho\phi_i(x)\phi_j(x)\mathrm{d}x \end{bmatrix} \tag{9}$$

$$k=\begin{bmatrix} 0 & 0 \\ 0 & \int_0^\ell EI\phi_{i,xx}\phi_{j,xx}\mathrm{d}x \end{bmatrix} \tag{10}$$

the vector b is null, except $b_1=1$ for the current experiment and

$$q=(\theta,q_1,q_2,\ldots,q_n)^T \tag{11}$$

Shape functions $\phi_i(x)$ are chosen herein to correspond to the eigenfunctions of a cantilever beam which are normalized relative to the mass density $\rho\ell$.[13] In this case, Eqs. (9) and (10) become

$$m=\begin{bmatrix} I_b & \int_0^\ell \rho x\phi_i(x)\mathrm{d}x \\ \int_0^\ell \rho x\phi_j(x)\mathrm{d}x & \rho\ell\hat{1} \end{bmatrix} \tag{12}$$

$$k=\begin{bmatrix} 0 & 0 \\ 0 & \rho\ell\omega^2 \end{bmatrix} \tag{13}$$

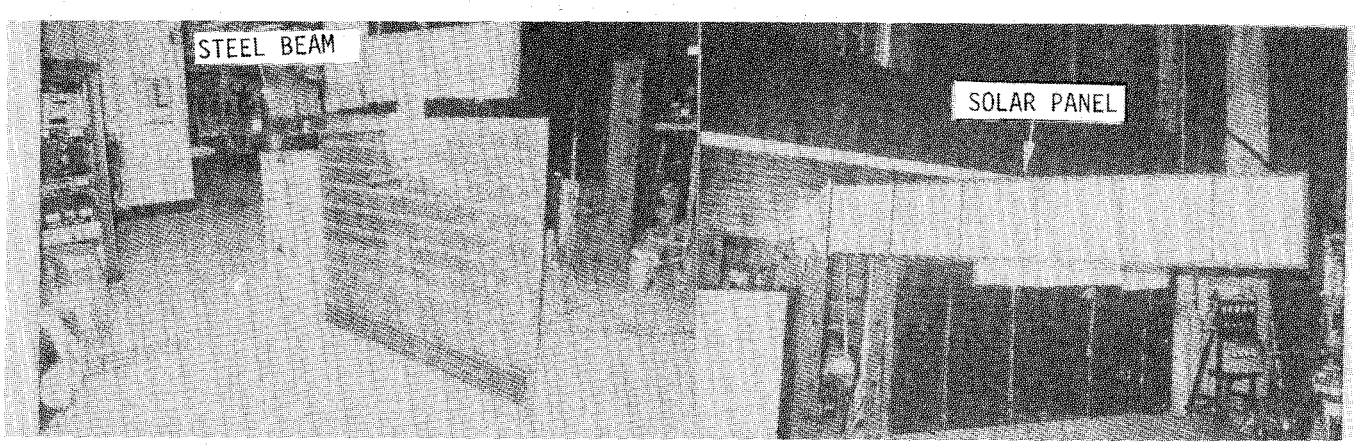

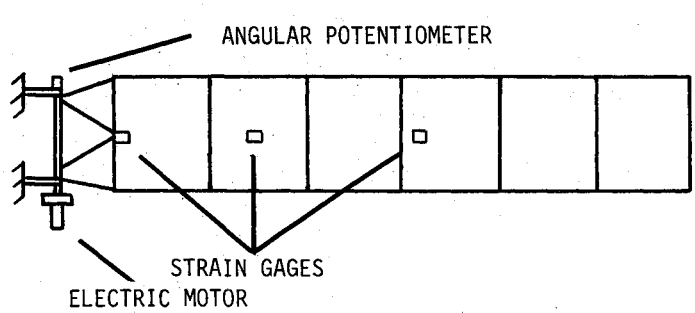

Fig. 1 Photographs of experimental models and diagram of typical setup.

where $\hat{1}$ is an $n \times n$ identity matrix and ω^2 is a diagonal matrix with elements ω_i as the frequencies corresponding to the shape functions ϕ_i.

Actuator Dynamics

The actuator used in this experiment is a dc electric motor, with a gear train and electromechanical brakes, which is modified for vacuum application.[15] The electric motor can be modeled as a standard armature circuit as shown in Fig. 2. Denote the armature resistance by R_a, the armature inductance by L_a, the back-EMF (electro-motive-force) constant by k_b, the armature current by i_a, and the motor shaft position by θ_m. Application of Kirchoff's loop law to the armature circuit yields

$$e_a = R_a i_a + L_a \dot{i}_a + k_b \dot{\theta}_m \tag{14}$$

where e_a is the applied voltage to the armature. The motor torque τ_m from the motor shaft with the motor torque constant k_t can be written as

$$\tau_m = k_t i_a \tag{15}$$

The torque τ_m will accelerate the motor, overcome the gear-train drag, and provide the torque to drive the beam. The motor dynamics thus become

$$I_m \ddot{\theta}_\omega + c_v \dot{\theta}_m + \tau_a = \tau_m = k_t i_a \tag{16}$$

where I_m is the motor and gear-train inertia, c_v is the gear-train viscous drag coefficient, and τ_a is the available torque from the motor shaft for the beam.

A gear train transforms power from the motor shaft to the output shaft while maintaining a definite ratio (overall gear ratio) between quantities such as position angle and torque. Let N_g denote the overall gear ratio. Quantities at the output shaft are related to those at the motor shaft by

$$\tau = N_g \tau_a, \qquad \theta_m = N_g \theta \tag{17}$$

Note that the motor electrical time constant ($L_a/R_a = 2.56 \times 10^{-3}$ s) in Eq. (14) is at least two orders of magnitude smaller than the driven system time constant. Substituting the armature current i_a from Eq. (14) into Eq. (16), ignoring the term L_a/R_a, and inserting Eq. (17) yield

$$\tau = (N_g k_t / R_a) e_a - (k_t k_b / R_a + c_v) N_g^2 \dot{\theta} - I_m N_g^2 \ddot{\theta} \tag{18}$$

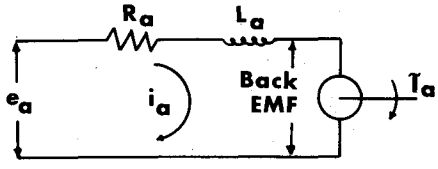

Fig. 2 Motor armature circuit.

where both e_a and θ are time-varying quantities. This is the torque available for maneuvering the beam.

Now, substituting Eq. (18) into Eq. (8) provides

$$\hat{m}\ddot{q} + d\dot{q} + kq = \hat{b}e_a \tag{19}$$

where

$$\hat{m} = m + \begin{bmatrix} I_m N_g^2 & 0 \\ 0 & 0 \end{bmatrix}$$

$$d = \begin{bmatrix} (k_t k_b / R_a + c_v) N_g^2 & 0 \\ 0 & 0 \end{bmatrix}$$

and

$$\hat{b} = \begin{bmatrix} N_g k_t / R_a \\ 0 \end{bmatrix}$$

This is the system equation including actuator dynamics. Equation (19) can be converted into a first-order system in terms of a standard state-variable format

$$\dot{q} = Aq + Be_a \tag{20}$$

where the state vector

$$q^T = (q^T, \dot{q}^T)$$

the state matrix

$$A = \begin{bmatrix} 0 & 1 \\ -\hat{m}^{-1}k & -\hat{m}^{-1}d \end{bmatrix}$$

and the control influence vector

$$B = \begin{bmatrix} 0 \\ \hat{m}^{-1}\hat{b} \end{bmatrix}$$

Measurement Characteristics of Sensors

The rotational angle is measured by two 10-turn rotary potentiometers connected in a bridge circuit.[16] One of the potentiometers is connected between the fixture holding the motor and the motor output shaft. The other potentiometer is used to balance the circuit output at the desired null position. The basic bridge circuit provides a method for making accurate measurements of dc voltage that is proportional to the rotational angle. Let e_p be the output voltage of the bridge circuit. The rotation angle and the output voltage are then related by

$$e_p = c_p \theta \tag{21}$$

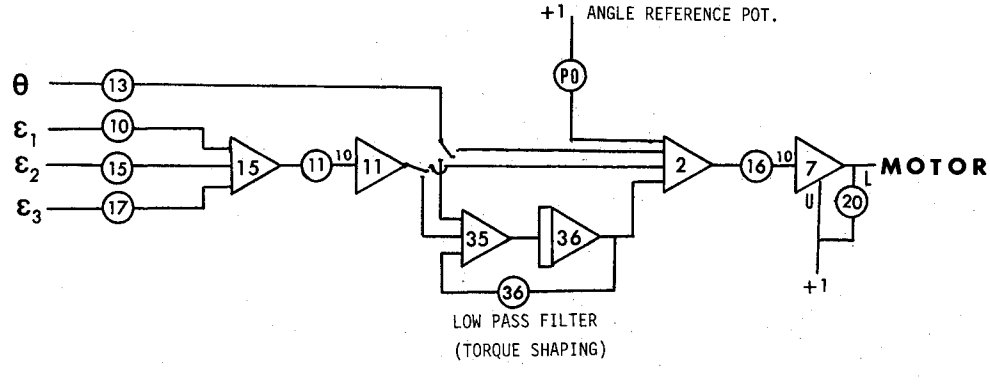

Fig. 3 Analog computer flowchart.

where c_p is the conversion factor that can be obtained by calibration.

The bending moment is measured by strain gages.[17] Strain is the measure of the change in length of the fibers for the bending deformation. The bending strain of the beam outer fibers is given by the relation[18]

$$\epsilon = hy_{,xx} \tag{22}$$

where h is the half-thickness of the beam. Note that $y_{,xx}$ is proportional to the bending moment for small deformation. Substitution of Eq. (6) into Eq. (22) produces

$$\epsilon = h\sum_{i=1}^{n}\phi_{i,xx}(x)q_i(t) \tag{23}$$

in which the bending deformation is approximated by assumed mode shapes.

A strain gage is a transducer that senses the amount of strain by a change in electrical resistance of the gage during mechanical deformation. As a rule, the strain gage is used in conjunction with a dc bridge that provides accurate voltage indications of small changes in gage resistance (i.e., strain). Denote the input voltage to the dc bridge by e_i and the output voltage by e_o. The strain and the output voltage with four active circuits arms are then related by

$$e_o = Ge_i\epsilon/4 \triangleq c_s\epsilon \tag{24}$$

where G is an empirical gage factor obtained from the manufacturer's specification or by calibration and c_s is a conversion factor between the strain ϵ and the output voltage e_o.

Combination of Eqs. (23) and (24) becomes

$$e_o = c_s\sum_{i=1}^{n}h\phi_{i,xx}(x)q_i(t) \tag{25}$$

This equation establishes the relationship between the generalized coordinates q_i and the output measurement e_o. If there are three sensors distributed along the beam located at x_1, x_2, x_3, Eqs. (21) and (25) can be combined and written in matrix form

$$e = \begin{bmatrix} e_1 \\ e_2 \\ e_3 \\ e_4 \end{bmatrix} \triangleq \begin{bmatrix} e_p \\ e_0(x_1) \\ e_o(x_2) \\ e_o(x_3) \end{bmatrix}$$

$$= \begin{bmatrix} c_p & 0 & \ldots & 0 \\ 0 & \multicolumn{3}{c}{\multirow{3}{*}{$\begin{bmatrix} \phi_{1,xx}(x_1),\ldots,\phi_{n,xx}(x_1) \\ \phi_{1,xx}(x_2),\ldots,\phi_{n,xx}(x_2) \\ \phi_{1,xx}(x_3),\ldots,\phi_{n,xx}(x_3) \end{bmatrix}$}} \\ 0 & c_sh & & \\ 0 & & & \end{bmatrix} \begin{bmatrix} \theta \\ q_1 \\ \vdots \\ q_n \end{bmatrix} \triangleq \hat{C}q \tag{26}$$

This is the measurement equation that relates the output voltage e to the generalized coordinates q_i. An active controller can then be designed using Eqs. (20) and (26).

Optimal Terminal Controller

The control design used in this experiment is the optimal terminal control law.[7,8] The optimal terminal control problem is formulated by finding the control input e_a to minimize the cost function

$$J = (1/2)\int_{t_0}^{t_f}(e^TQe + e_a^TRe_a)\,dt \tag{27}$$

for the system of order $2n+2$ [see Eq. (20)]

$$\dot{q} = Aq + Be_a, \text{ given } q(t_0) \tag{28}$$

with output measurements [see Eq. (26)]

$$e = \hat{C}q = [\hat{C},\ 0]q \triangleq Cq \tag{29}$$

subject to the specified terminal constraints

$$\psi = He(t_f) \tag{30}$$

where C is the measurement influence matrix, $Q \geq 0$ an output state weighting matrix, $R > 0$ a control weighting constant, H a constant matrix of rank 4, and ψ a constant vector. It can be easily proved that (A,B) is stabilizable. Assume that $(CQ^{1/2}, A)$ is observable, and the system is completely output-controllable with respect to HC by properly choosing the matrices Q and H.

Let the square constant matrix P_{ss} satisfy the steady-state Riccati equation

$$A^TP_{ss} + P_{ss}A - P_{ss}BR^{-1}B^TP_{ss} + C^TQC = 0 \tag{31}$$

and

$$\bar{A} = A - BR^{-1}B^TP_{ss} \tag{32}$$

be a stability matrix. The feedback law for $t_0 \leq t < t_f$ that minimizes the cost function J with constraints is

$$e_a = -R^{-1}B^T[(P_{ss} + Z_m^{-1}(t))q(t) + S_m(t)\psi] \tag{33}$$

where the transient feedback matrix $Z_m(t)$ and the terminal feedback matrix $S_m(t)$ satisfy the following equations:

$$\dot{Z}_m = Z_m\bar{A}^T + AZ_m - BR^{-1}B \tag{34}$$

$$\dot{S}_m = [\bar{A}^T + Z_m^{-1}BR^{-1}B^T]S_m \tag{35}$$

respectively, subject to the terminal conditions

$$Z_m(t_f) = -P_{ss}^{-1} + P_{ss}^{-1}C^TH^TWHCP_{ss}^{-1} \tag{36}$$

and

$$Z_m(t_f)S_m(t_f) = -P_{ss}^{-1}C^TH^TW, \quad W^{-1} = HCP_{ss}^{-1}C^TH^T \tag{37}$$

The solution of Eq. (34) subject to the boundary condition (36) is given by

$$Z_m(t) = Z_{ss} + \exp[\bar{A}(t-t_f)][Z_m(t_f) - Z_{ss}]\exp[\bar{A}^T(t-t_f)] \tag{38}$$

where Z_{ss} satisfies the algebraic Lyapunov equation[7,8]

$$\bar{A}Z_{ss} + Z_{ss}\bar{A}^T = BR^{-1}B^T \tag{39}$$

For the system with assumptions as in this paper, the transient feedback matrix $Z_m^{-1}(t)$ exists for $t_o \leq t < t_f$.

$$Z_m^{-1}(t) = \exp[\bar{A}^T(t_f-t)]\{\exp[\bar{A}(t_f-t)]Z_{ss}\exp[\bar{A}^T(t_f-t)] + Z_m(t_f) - Z_{ss}\}^{-1}\exp[\bar{A}(t_f-t)] \tag{40}$$

Combination of Eqs. (35) and (40) then produces

$$S_m(t) = -\{\exp[\bar{A}(t_f-t)]Z_{ss}\exp[\bar{A}^T(t_f-t)] + Z_m(t_f) - Z_{ss}\}^{-1}\exp[\bar{A}(t_f-t)]P_{ss}^{-1}C^TH^TW \tag{41}$$

The preceding results lead to solutions for the control law (33) with any given state and terminal constraints. First, obtain the solutions P_{ss}, $Z_m^{-1}(t)$, and $S_m(t)$, respectively, from Eqs. (31), (40), and (41) at any time $t_0 \leq t t_f$. Substitution of these solutions into Eq. (33) will then determine the control input $e_a(t)$.

Observation of Eqs. (40) and (41) reveals that the time-varying matrices $Z_m^{-1}(t)$ and $S_m(t)$ essentially depend on the stability matrix $\bar{A}$ and the time period $t_f - t$. The more asymptotically stable the matrix $\bar{A}$, the smaller the magnitude of the entries of these time-varying matrices. In other words, the time-varying matrices $Z_m^{-1}(t)$ and $S_m(t)$ become less important when the eigenvalues of the matrix $\bar{A}$ move farther to the left in the complex plane. The control input $e_a(t)$ in this case will then be determined essentially by the constant square matrix P_{ss} until time closely approaches t_f. Equations (31) and (32) imply that proper selection of the weighting terms Q and R will give the desired eigenvalues of the matrix $\bar{A}$. Therefore, the weighting matrices Q and R play a major role in determining the relative importance of the constant feedback and the time-varying feedback shown in Eq. (33) for the control input $e_a(t)$.

Equation (33) is a full state feedback law that requires a state estimator to determine the state vector $q(t)$. Assuming that the output measurement e in Eq. (26) is differentiable, the state vector $q(t)$ can be determined by

$$q = \begin{bmatrix} q \\ \dot{q} \end{bmatrix} = \begin{bmatrix} \hat{C}^{-1} & 0 \\ 0 & \hat{C}^{-1} \end{bmatrix} \begin{bmatrix} e \\ \dot{e} \end{bmatrix} \triangleq C^{-1} e \tag{42}$$

Substituting Eq. (42) into Eq. (33) yields

$$e_a(t) = -R^{-1}B^T[(P_{ss} + Z_m^{-1}(t))C^{-1}e + S_m(t)\psi]$$
$$\triangleq [g_{ss} + g(t)]e + g_s(t)\psi \tag{43}$$

where the vector g_{ss} is the steady-state constant gain for the output measurement vector e. This is equivalent to an output feedback law. Note that other methods[19] may be used to compute the output feedback gains, particularly when some inequality constraints are imposed.

It is generally inadvisable to differentiate a measurement signal because noise effects are greatly magnified. However, if the gains for the differentiated signals are significantly smaller than those for the measured signals, they may be neglected without degrading the performance of the control law. Observe that differentiation of signals from the potentiometer and strain gages provides the angular velocity and strain rates. Feeding back velocity information basically provides damping for the system. The amount of overall damping for a control system is determined by the performance requirements including the terminal time, the pointing precision, etc. When a significant amount of damping already exists in the system through sources such as the motor back-EMF to satisfy a specified performance requirement, the velocity feedback becomes insignificant for a controller design. Indeed, with the aid of the damping term d in Eq. (19) due to the actuator dynamics, it is shown in the discussion of results that a robust controller design can be developed without velocity feedback.

Discussion of Results

Different controller design strategies are implemented on two different models, including a steel beam and a simulated solar panel. For each case the approach taken is as follows. First, a reduced-order model is obtained using the first three bending modes of a cantilever beam and a rigid body mode identified as the root angle. Second, this model is used in the evaluation of the control law (gains in the feedback loop) as previously shown in Eq. (43). Third, to assess the actual performance with real hardware, this control law is implemented in the laboratory using an analog computer.

Amplifiers are used to receive signals from sensors and supply signals for the actuator. The output of the potentiometer is amplified by 20, using one channel of the amplifier. The amplifer gain is set to 100 for all three strain gages. An EAI 2000 analog computer is used to combine amplified signals into a feedback control signal. The circuit used to provide the feedback control law [Eq. (43)] is shown in Fig. 3. The amplifier numbers are given for completeness. The input signal for the electric motor from the EAI 2000 analog computer is amplified by 2.7. It is important to note that the units used in the analog computer, called machine units, are one-tenth of the actual input and output units.

Table 1 shows the electric motor, strain gage, steel beam, and solar panel parameters used in the analytical simulations. Some of the motor parameters are inferred from the motor specification sheets. Others, such as the back-EMF (k_b), viscous drag coefficient c_v due to lubrication, and the potentiometer conversion factor c_p, are experimentally determined. The conversion factors c_p and c_s are expressed in terms of the EAI 2000 machine unit. The viscous drag is estimated to be 4% of the back-EMF term shown in Eq. (18). The back-EMF and the viscous drag are the only two energy-dissipation mechanisms included in the equations of motions. Table 2 shows weighting matrices used in Eq. (27) to compute the control laws, which are shown in Table 3. Note that the metric unit system has been used to compute the system equation and the control laws for the solar panel experiment. Since the root angle is not strongly coupled with the flexible modes in the state equation, the weighting matrices can be approximately determined by desired closed-loop system eigenvalues using an uncoupled state equation for the root angle.

Table 1 Model parameters

Motor	Strain gages
$k_t = 0.205$ in.-lbf/amp (0.023 N-m/amp)	$G = 2.115$
$k_b = 0.031$ V-s/rad	$e_i = 5.0$ V
$R_a = 3.7$ ohm	
$L_a = 10$ mh	
$I_m = 3.56 \times 10^{-5}$ lbf-in.-s^2 (4.02×10^{-6} N-m-s^2)	
$N_g = 941$	
Steel beam	Solar panel (aluminum/honeycomb)
$\ell = 39.5$ in. (1.0 m)	$\ell = 12.8$ ft (3.9 m)
$EI = 246.0$ lbf-in.^{2} (0.71 N-m^2)	$EI = 1.44 \times 10^5$ lbf-in.^{2} (328.3 N-m^2)
$\rho = 6.95 \times 10^{-5}$ lbf/in. (0.124 kg/m)	$\rho = 0.173$ lbf/in. (3.08 kg/m)
$h = 0.016$ in. (0.04 cm)	$h = 0.13$ in. (0.65 cm)
Conversion factors (machine units)	
$c_p = 0.17$ V/rad	
$c_s = 2.64$ V/in./in.	

Four cases from the experiment are discussed. They are identified by their approximate slew rate, slew angle, and laboratory model used. The first case, shown in Fig. 4, is a 45-deg slew in 1.5 s. The model used is the steel beam. The sensor information used to compute the control signal is across the top of Fig. 4, while the response output is indicated vertically. For example, the first column shows the measured angle, root strain, and control torque when feeding back only the angle information. The second column shows the measured angle, root strain, and control torque for the same maneuver using both angle and root strain feedback. The vertical axis is in volts, which can be converted to physical units using the conversion factors in Table 1.

If no strain information is used, the 45-deg maneuver can be achieved with no overshoot in the root angle but with a lot of beam residual motion as shown by the strain output. The beam kinetic energy after reaching the specified angle does not overcome the mechanical advantage of the gear train. In other words, the beam vibration does not affect the motion of the motor. The large gear ratio and small moment of inertia of the beam are principal contributors to this phenomenon. If a load is applied at the tip of the beam, for example, the motor will not rotate. This phenomenon can be taken into account mathematically by neglecting the causal effect of the beam modal accelerations on the motor acceleration. This can be done by grounding the last n terms in the first row of the mass matrix m in Eq. (12). This simplified model has been used to compute the control law and conduct the modal parameter analysis for the steel beam. However, this decoupling phenomenon does not occur for the solar panel model because of its greater inertia.

When the root strain is used, along with the angle information, some overshoot is observed in the second column of Fig. 4, but the residual motion is substantially reduced. Furthermore, when all three strains are used, the maximum peak strain is reduced slightly more. The addition of the root strain feedback in the control law proves to be a very effective factor for reducing residual vibration. It is easy to explain by considering that the first bending mode is excited the most and that the highest strain for that mode occurs at the root. The control law and gain coefficients are shown in Table 3. Velocity feedback gains are neglected since they are relatively small. This is contributed by the significant damping term [Eq. (19)] induced by the large motor back-EMF.

The second case shown in Fig. 5 corresponds to a 30-deg slew of the solar panel in 3.5 s. When only angle feedback is used, some overshoot for the angle measurement is observed in the first column in contrast to corresponding results for the

Table 2 Weighting matrices for sample maneuvers

	Weighting matrices
Steel beam	$Q = \text{diag}\,[10^8, 10^2, 1, 1, 1, 1, 1, 1] \times 10^{-6}$ $R = 2.718 \times 10^3$
Solar panel	$Q = \text{diag}\,[10^7, 10^6, 1, 1, 1, 1, 1, 1] \times 10^{-6}$ $R = 34.7$
Solar panel (critically damped)	$Q = \text{diag}\,[10^5, 10^4, 1, 1, 1, 1, 1, 1] \times 10^{-6}$ $R = 34.7$

Table 3 Controller design gains

Control law	$e_a = g_{ss1}e_1 + g_{ss2}e_2 + g_{ss3}e_3 + g_{ss4}e_4$			
Steel beam	$g_{ss1} = -14.82$	$g_{ss2} = 185.20$	$g_{ss3} = 44.99$	$g_{ss4} = -25.43$
Solar panel	$g_{ss1} = -43.48$	$g_{ss2} = 64.89$	$g_{ss3} = 117.70$	$g_{ss4} = 0.55$
Torque shaping constant	$= -6.5$			
Solar panel (critically damped)	$g_{ss1} = -4.35$	$g_{ss2} = 27.22$	$g_{ss3} = 39.96$	$g_{ss4} = 8.06$

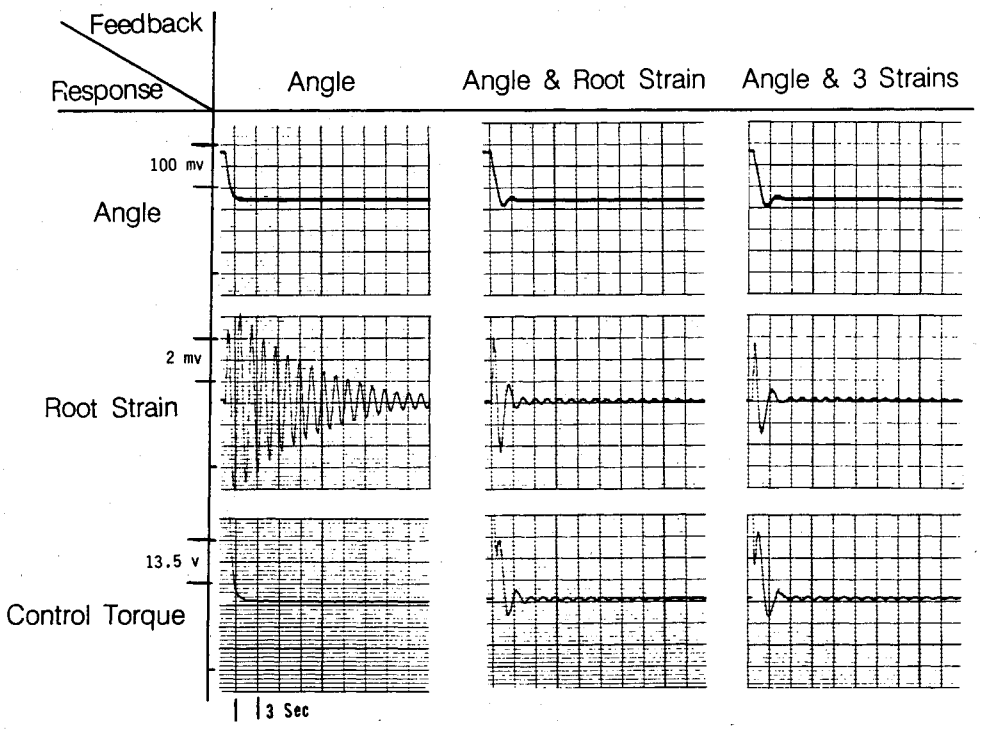

Fig. 4 Histories of steel beam 45-deg slew in 1.5 s.

steel beam in Fig. 4. This is because the solar panel kinetic energy after the maneuver is completed is able to overcome the mechanical advantage of the gear train. Moreover, the control torque appears to be a square signal. This is due to backlash in the gear train, which allows the panel to oscillate about a nominal position, with no apparent change in the root angle orientation. This is a nonlinear effect that was not accounted for in the analytical simulations. The addition of strain feedback improves the closed-loop transient response and produces a less irregular control signal. The control gains for this case also appear in Table 3.

Using the analytical model, the control gains can be manipulated to approximate a critically damped system. The third case shown in Fig. 6 presents the implementation of this control law for the solar panel. The slew rate is 30 deg in 4.5 s. The rate has to be decreased because no solution exists that will produce a faster slew rate and still approximate a critically damped system. Some overshoot is still observed because of model and actuator uncertainties, but nevertheless the overall closed-loop response is improved over any of the other cases shown. Further reduction of the peak strain is obtained when

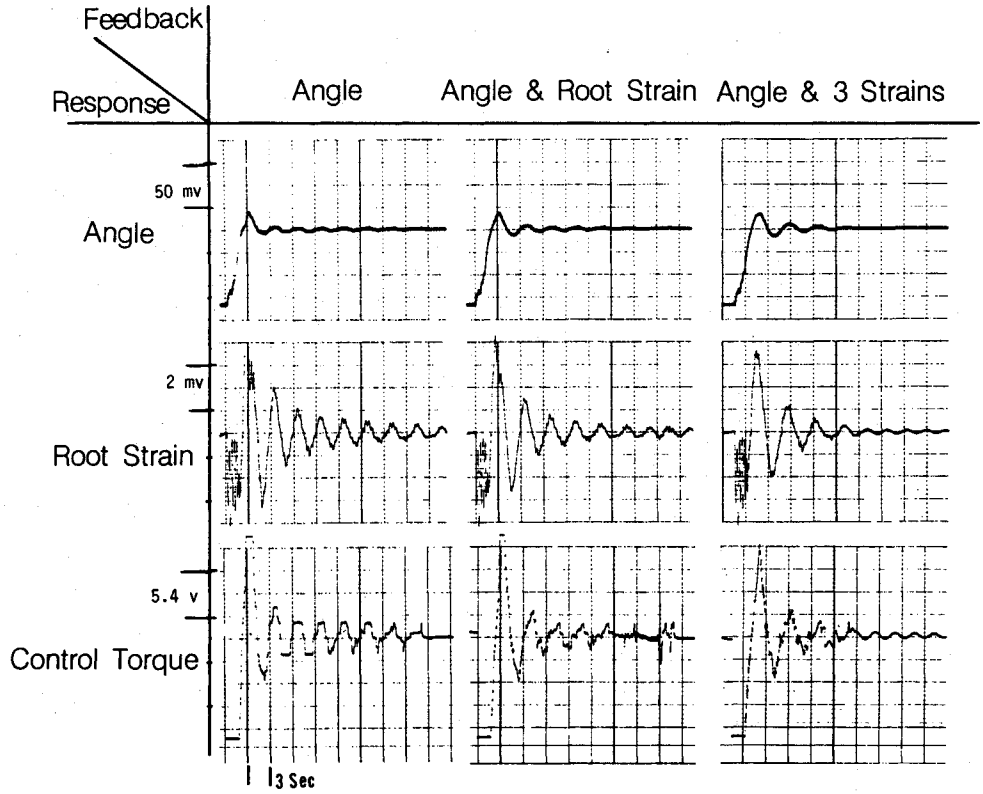

Fig. 5 Histories of solar panel 30-deg slew in 3.5 s.

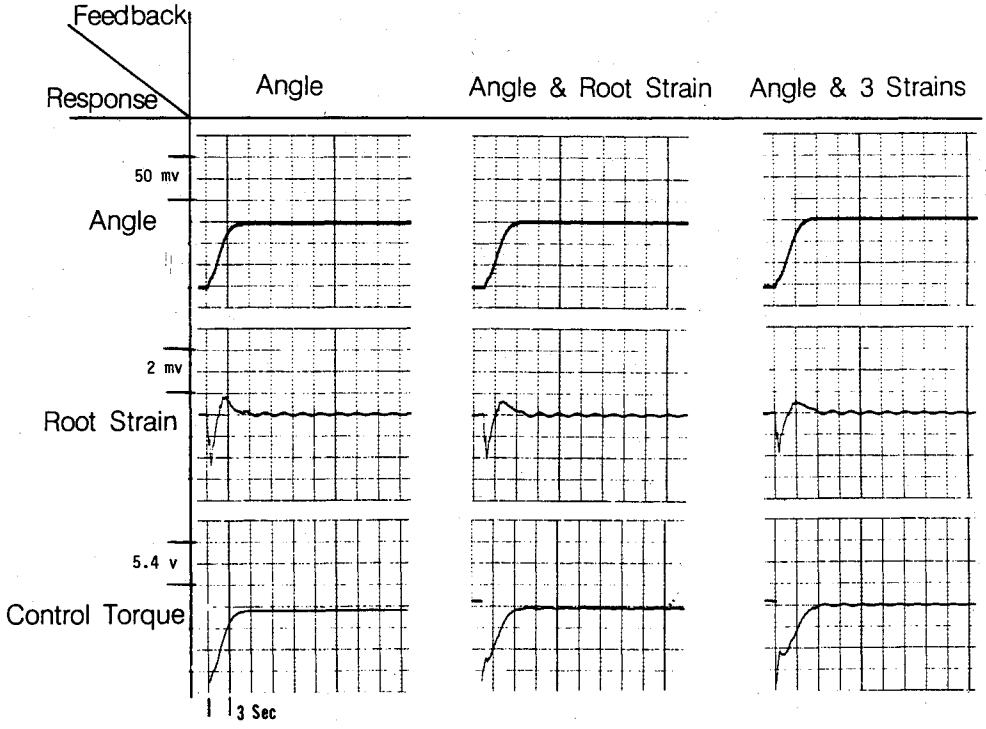

Fig. 6 Histories of solar panel 30-deg slew in 4.5 s, critically damped.

Table 4 Steel beam results comparison

		Analysis		Experiment	
Feedback	Modes	Damping ratio, %	Frequency, Hz	Damping ratio, %	Frequency, Hz
Angle	1	0.0	0.67	2.61	0.61
	2	0.0	4.23	1.05	4.18
	3	0.0	11.8		
Angle & strains	1	6.40	0.59	17.5	0.55
	2	5.89	4.14	2.98	3.93
	3	2.27	11.8		

Table 5 Solar panel results comparison

		Analysis		Experiment	
Feedback	Modes	Damping ratio, %	Frequency, Hz	Damping ratio, %	Frequency, Hz
Angle	1	0.52	0.33	4.44	0.32
	2	2.05	2.10	5.25	2.75
	3	1.83	6.02		
Angle & strains	1	1.32	0.30	15.57	0.25
	2	2.90	2.05	1.97	2.19
	3	1.76	6.00		

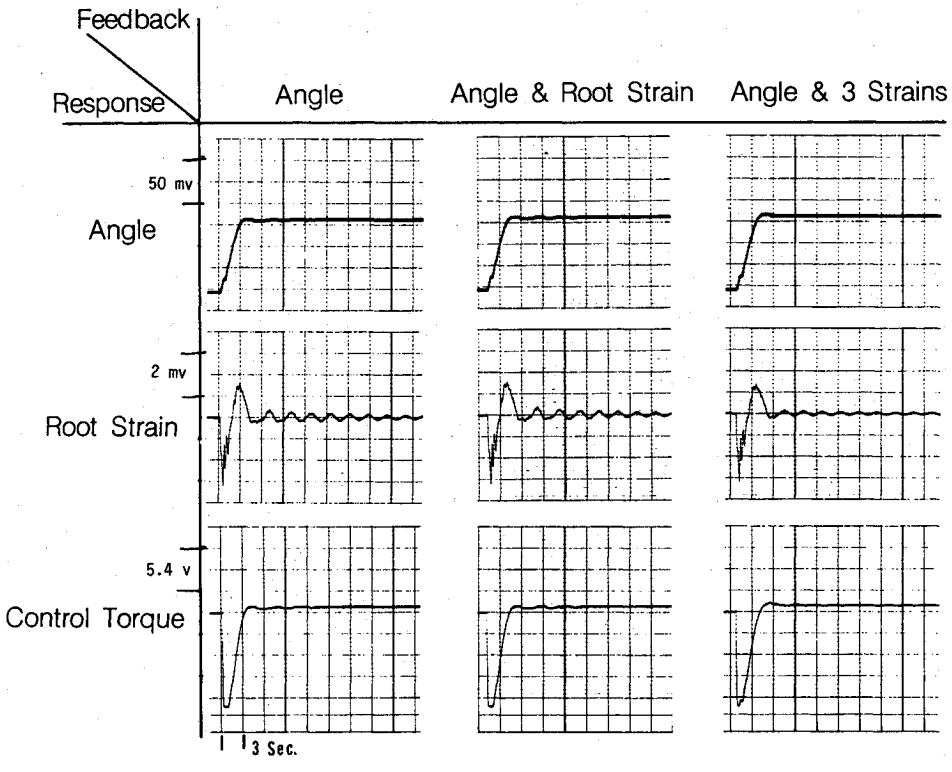

Fig. 7 Histories of solar panel 30-deg slew in 3.5 s with torque shaping.

strain information is also used. The gain settings are shown in Table 3.

The last case shown in Fig. 7 is the implementation of torque shaping for a 30-deg slew in a 3.5-s time period. The control gains are the same as those used in case 2 with the addition of a torque shaping constant. The torque shaping is accomplished by augmenting the system states [Eq. (28)] to include the control torque e_a and penalizing the derivative of the torque in the cost function [Eq. (27)]. The reader is directed to Refs. 7-8 for more information. The torque shaping constant is defined as the gain coefficient for the state e_a shown in the closed-loop torque state equation, which, in this case, is a first-order differential equation. Torque shaping acts essentially as a low-pass filter reducing any high-frequency component that might result from the feedback information. The performance of the system with torque shaping is tremendously improved over case 2. Because of a smoother control signal, very small residual vibration is observed at the end of the maneuver. The inclusion of strain information produced a slight reduction in the peak strain but is not very significant. Note that by adding the torque shaping, a faster slew rate is achieved than in the critically damped case, with similar performance. This is considered to be a very promising technique for control implementation with a very small increment in control hardware.

A comparison of the analytically predicted closed-loop eigenvalues of the steel beam with experimentally determined eigenvalues is shown in Table 4. To extract the modal information from the laboratory data, an eigensystem realization algorithm[20,21] is used. The upper half of Table 4 shows the frequency and damping values when using angle feedback only. Since the upper part of the coupling terms between the flexible modes and the root angle was removed from the analytical model, the predicted damping is zero. However, the experimental results show 2% modal damping in the first mode and 1% damping in the second mode due to air drag. No identification of the third mode is possible because of its low contribution. It is recognized that damping estimation from experimental data with air drag effect is sometimes a very difficult problem. The results presented herein are average values for different identification trials. The first bending mode frequency is about 10% higher than the theoretical value. This is attributed to slack in the clamp fixture and motor backlash in the laboratory model which result in a slightly different boundary condition. The lower half of Table 4 shows the results using all three strain feedbacks in addition to the angle. The analytically predicted frequencies are again within 10% of the experimental frequencies. The predicted modal damping for the first mode is considerably lower than the experimental value. This is because of air damping, model uncertainties, and motor/gear-train backlash (nonlinearities), which serve as energy dissipation devices that are not modeled.

Table 5 shows a comparison of the solar panel experiment results with the analytical simulations for the cases shown in

Fig. 5. The upper half contains the results using only angle feedback without torque shaping. Note that because of the inclusion of coupling terms, the predicted damping values are greater than zero in contrast to the steel beam. A physical interpretation is that when these terms are included, the bending energy is transferred to the motor, where all the energy dissipation takes place. The bottom part of Table 5 shows the results using all strains as well as angle feedback. The first identified frequency is lower than the predicted one (due to the clamp fixture). The identified damping for the first bending mode is about 15 times the predicted values. This is expected because of the large panel area, which receives significant air drag.

All the results presented thus far are related only to the constant stability matrix $\bar{A}$, which is derived from the constant gain feedback shown in the control torque equation (33). To satisfy the specified terminal states precisely, the time-varying gain feedback is required theoretically in addition to the constant feedback. However, as discussed earlier, when the slewing time is longer than the time constant of the strongly excited modes in the stability matrix, the time-varying feedback becomes negligible in practical cases. To prove this theoretical observation, a time-varying gain has been generated from a computer simulation using Eqs. (40), (41), and (43). It has been shown, from the simulation for slewing the steel beam with the same slew rate as before, that the additional time-varying feedback does not significantly improve performance. When a faster slew is performed using the same stability matrix, it is necessary to use the time-varying feedback to meet the requirement. From very limited experimental results in controlling the vibrational motion of flexible structures, the additional time-varying feedback seems more sensitive to the system uncertainty than the constant feedback alone. It appears that relying more on the constant feedback than on the time-varying feedback is likely to produce a more robust controller for the terminal control problem. This issue requires more research on both theoretical and experimental bases for structures as well as controls, including parameter estimation[22] to help identify the sources of uncertainties.

Concluding Remarks

A slewing control for flexible structures has been experimentally demonstrated. The controller successfully performed a large-angle maneuver and simultaneously damped out flexible modes at the end of the maneuver. An optimal terminal control law was used to compute the feedback gains. Several different controller designs were evaluated and discussed in detail in terms of time responses and modal parameters. Satisfactory agreement was achieved between experimental measurements and theoretical predictions. The nonlinear effects due to large bending deflection during actual slewing maneuvers did not cause significant changes in predicted characteristics of the control laws, which were designed using linear control theory.

However, the time to damp flexible motion was less than predicted in simulation because the design model did not take air drag into account. The difference may be dramatic, particularly for large initial displacement with high velocities. Research should be done to assess the effects of air drag on slewing control experiments for flexible structures.

To minimize the excitation of flexible modes, a low-pass filter was used to shape the control torque input. Torque shaping was proved to be beneficial for fast slewing maneuvers. Because of a smooth control signal, the system nonlinear effects were minimized, and thus the system performance was considerably improved.

The electric motor and strain gages appear to be effective and inexpensive hardware for controller implementation. The back-EMF of the electric motor provided significant motor damping. Through the feedback of root angle and root strain information, the motor damping is actively and adequately distributed to the system. Therefore, the electric motor with high back-EMF not only helps develop a robust controller but also minimizes the need of velocity feedback of vibrational motion. However, it is difficult to characterize the electric motor to measure accurately the back-EMF value.

References

[1]Balas, M. J., "Trends in Large Space Structure Control Theory: Fondest Hopes, Wildest Dreams," *IEEE Transactions on Automatic Controls*, Vol. 27, 1982, pp. 552-535.

[2]Schaechter, D. B., "Hardware Demonstration of Flexible Beam Control," *Journal of Guidance, Control, and Dynamics*, Vol. 5, Jan.-Feb. 1982, pp. 48-53.

[3]Hallauer, W. L. Jr., Skidmore, G. R., and Gehling, R. N., "Modal-Space Active Damping of a Plane Grid: Experiment and Theory," *Journal of Guidance, Control, and Dynamics*, Vol. 8, May-June 1985, pp. 366-373.

[4]Meirovitch, L., Baruh, H., Montgomery, R. C., and Williams, J. P., "Nonlinear Natural Control of an Experimental Beam," *Journal of Guidance, Control, and Dynamics*, Vol. 7, July-Aug. 1984, pp. 437-442.

[5]Schafer, B. E. and Holzach, H., "Experimental Research on Flexible Modal Control," AIAA Paper 84-1020, May 1984.

[6]Breakwell, J. A., "Optimal Feedback Slewing of Flexible Spacecraft," *Journal of Guidance and Control*, Vol. 4, Sept.-Oct. 1981, pp. 472-479.

[7]Juang, J.-N., Turner, J. D., and Chun, H. M., "Closed-Form Solutions of Control Gains for a Terminal Controller," *Journal of Guidance, Control, and Dynamics*, Vol. 8, Jan.-Feb. 1985, pp. 38-43.

[8]Juang, J.-N., Turner, J. D., and Chun, H. M., "Closed-Form Solutions for a Class of Optimal Quadratic Regulator Problems with Terminal Constraints," *Proceedings of the AIAA Dynamics Specialist Conference*, Palm Springs, CA, May 17-18, 1984; *ASME Journal of Dynamics, Measurements and Control*, Vol. 108, March 1986, pp. 44-48.

[9]Belvin, W. K. and Edighoffer, H. H., "Experimental and Analytical Generic Space Station Dynamic Models," NASA TM-87696, March 1986.

[10]Meirovitch, L., *Analytic Methods in Vibrations*, Macmillan, New York, 1971.

[11]Juang, J.-N., "Optimal Design of a Passive Vibration Absorber for a Truss Beam," *Journal of Guidance, Control, and Dynamics*, Vol. 7, Nov.-Dec. 1984, pp. 733-739.

[12]Juang, J.-N. and Balas, M. J., "Dynamics and Control of Large Spinning Spacecraft," *The Journal of the Astronautical Sciences*, Vol. 28, Jan.-March 1980, pp. 31-48.

[13]Meirovitch, L. and Juang, J.-N., "Natural Modes of Oscillation of Rotating Flexible Structures About a Nontrivial Equilibrium," *Journal of Spacecraft and Rockets*, Vol. 13, Jan. 1976, pp. 37-44.

[14]Bishop, R. E. D. and Johnson, D. C., *The Mechanics of Vibration*, Cambridge University Press, London, England, 1960.

[15]TRW Globe Motors, D-300 Division of TRW Inc., Dayton, OH.

[16]Malvino, A. P., *Electronic Instrumentation Fundamentals*, McGraw-Hill Book Company, New York, 1967.

[17]Perry, C. C. and Lissner, H. R., *The Strain Gage Primer*, 2nd ed., McGraw-Hill Book Company, New York, 1962.

[18]Timoshenko, S. P. and Goodier, J. N., *Theory of Elasticity*, 3d ed., McGraw-Hill Book Company, New York, 1970.

[19]Horta, L. G., Juang, J.-N., and Junkins, J. L., "A Sequential Linear Optimization Approach for Controller Design," *Proceedings of AIAA Guidance, Navigation and Control Conference*, Snowmass, CO, Aug. 1985, pp. 725-731; *Journal of Guidance, Control, and Dynamics* (to be published).

[20]Juang, J.-N. and Pappa, R. S., "An Eigensystem Realization Algorithm for Modal Parameter Identification and Model Reduction," *Journal of Guidance, Control, and Dynamics*, Vol. 8, Sept.-Oct. 1985, pp. 620-627.

[21]Juang, J.-N. and Pappa, R. S., "Effects of Noise on Modal Parameters Identified by the Eigensystem Realization Algorithm," *Journal of Guidance, Control, and Dynamics*, Vol. 9, May-June 1986, pp. 294-303.

[22]Banks, H. T. and Crowley, J. M., "Parameter Identification in Continuum Models," *The Journal of the Astronautical Sciences*, Vol. 33, Jan.-March 1985, pp. 71-83.